International Journal of Interdisciplinary Innovative Research & Development (IJIIRD)
ISSN: 2456-236X
Vol. 10 Issue 01 | 2025

Fractional Order Notch Filter for Power Quality Enhancement in Grid-Integrated Solar Photovoltaic with Quasi Z-Source Multilevel Inverter

Vijay Sitaram Pawar[1], Dr. Prashant J. Gaidhane[2]
[1] Associate Professor, Electrical Engineering Department, Government Engineering College, Jalgaon, Maharashtra 425001, India
[2] Associate Professor, Instrumentation Engineering Department, Government College of Engineering, Jalgaon, Maharashtra 425001, India

DOI: 10.5281/zenodo.16309424

ABSTRACT

This research discusses an improved control strategy for using a Fractional Order Notch Filter (FONF) with a Quasi-Z-Source Cascaded H-Bridge Multilevel Inverter (QZS-CHBMLI) in order to improve power quality in on-grid solar photovoltaic systems. Solar photovoltaic systems are mostly integrating into the power grid in line with the increasing demand for clean energy, voltage fluctuation, harmonics distortion, and instability problems affecting system performance. The combined FONF-and-Crested Porcupine Optimizer (CPO) configuration considers those issues by further enhancing the potential noise mitigation and dynamic control. The forms of FONF filter out harmonics while ensuring stability in the system, and the CPO optimize the filter parameters so that efficiency is maximized for varying operation conditions. The multichannel inverter is capable of converting direct current into alternating current and offers output at low total harmonic distortion. Results from simulation and experiments attest to the very performance of the proposed approach with notable total harmonic distortion reduction as well as voltage stability improvement under dynamic load and environmental fluctuation. This research establishes the ground for control strategies based on FONF for improving the performance of renewable energy systems for grid-connected solar- photovoltaic applications.

Keyword: - Solar Photovoltaic, Multilevel Inverter, voltage fluctuation, harmonics distortion, power grid, Noise Mitigation, Power Quality Enhancement

1. Introduction

At present, renewable energy sources, such as wind power systems and solar Photovoltaic (PV), are critical to electricity generation, depending heavily on the current and forecasted weather conditions. PV systems have a great number of capabilities, although numerous problems - including grid interfacing, power conversion, and electric loads - cause power quality interruptions [2]. Battery management systems are solutions for energy storage systems in power issues [3]. In the typical grid configurations, sunlight is converted to electrical energy using a low-frequency transformer inserted after inverter and before AC grid [4]. It proposes three-phase grid-connected photovoltaic system functioned by a new three-level Neutral-Point-Clamped (NPC) inverter integrated interfaced through a high-gain DC converter interleaved with the inverter for enhancing power performance [5]. Multilevel inverters are promising providing a high-power output during fluctuation [6]. Therefore, this helps build a very diversified and strong system to generate energy, thus creating a much more stable and reliable electricity supply [7]. For example, grid integration of PV systems commonly used the three-phase modular multilevel inverter which utilized a Service-Oriented Architecture (SOA)-optimized controller and grid voltage to manage active and reactive power [8]. Alternatively, a one-stage converter topology without transformer or without additional active switch is known at present as Z-Source Inverter (ZSI) [9]. Filters improve power quality by reducing harmonics and distortion and increasing performance of power factor. With all these new developments, renewable energy is indeed going to improve the overall grid system efficiency and reliability [10].

1.1 Literature Survey

Literature works have previously existed in the literatures which are based on the PV power generation forecasting using various methodologies in [11-15].

Srinath N.S., et.al [11] have devised a control scheme that delivers both active and reactive power from the solar system to the grid while preserving power quality from all the problems such as harmonic generation, power-factor deterioration, load imbalance, etc.

Anusha G., et.al [12] focuses on the hurdles faced in injecting Multilevel Inverters (MLIs) into Renewable Energy Systems (RES), highlighting that there was a difficult control and coordination process needed for efficient operation.
Bhimraj M.R., et.al [13] has introduced an innovative smart detection technique for power quality events that identifies and classifies these events in power in the most accurate way as a crucial step toward effective mitigation.
Kumar P.S., et.al [14] presented the method of Model Predictive Voltage (MPV) control to enable both effective power interchanges between AC and DC sub grid segments and co-ordinated control of the power fluctuation.
Rajamallaiah A., et.al [15] explained a new control strategy that aims to enhance the Direct Current Regulation (DCR) in grid connected two-level inverters with Inductor-Capacitor-Inductor (LCL) filters..

2. Proposed Framework

The integrated solar PV system illustrated in the Figure 1 is optimized for effective energy conversion and supply within the grid and local loads. The solar PV generates DC power, maximized through Maximum Power Point Tracking (MPPT), and boosted using a boost converter. The high-voltage DC is then transformed into high-quality AC via a QZS-CHBMLI, which ensures low harmonic distortion and increased power quality. An advanced control system, comprising FONF as well as CPO has been designed and implemented to control dynamics of the system through parameter optimization and behavioural stability. The firing pulses generated for the Insulated Gate Bipolar Transistor (IGBT) of the inverter realize the desired outputs of AC precisely. The system thus provides AC for the grid, as well as for some local loads, thus promoting the efficient use of energy in a stable noise-reduced environment with effective performance. The mathematical modelling of solar PV, boost converter and power grid is given in [16], [17].

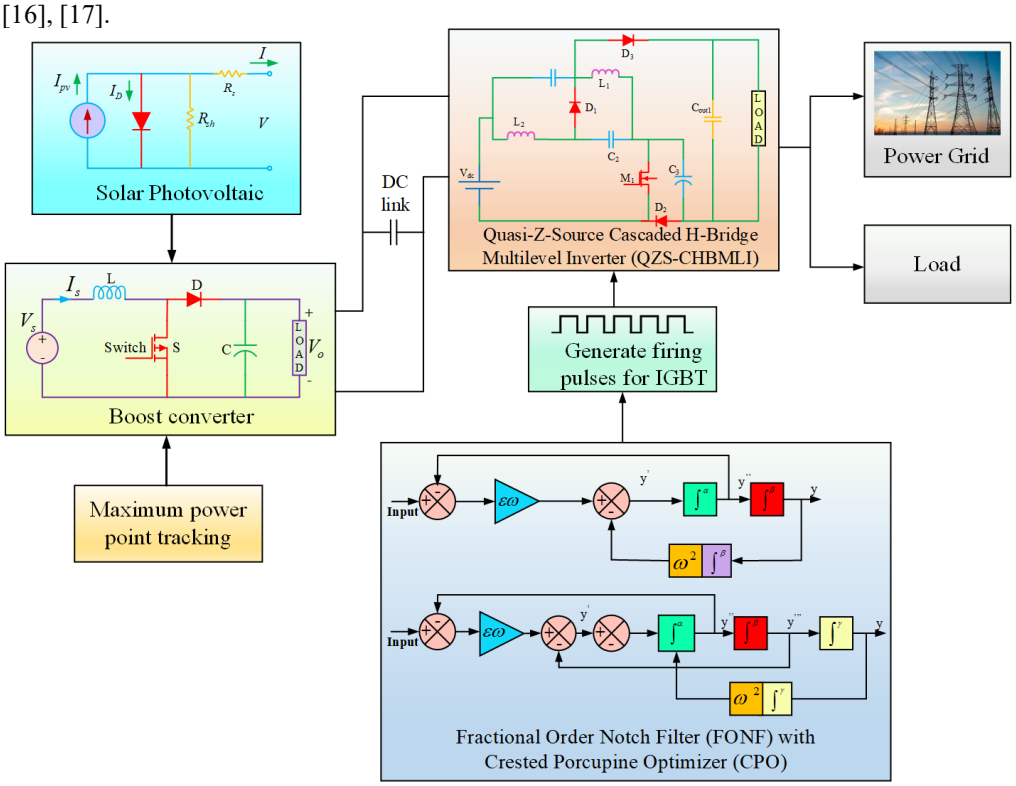

Fig -1: Block diagram for power quality enhancement in grid-integrated solar PV with proposed inverter

2.1 Mathematical Modelling of Quasi-Z-Source Cascaded H-Bridge Multilevel Inverter (QZS-CHBMLI)

The QZS-CHBMLI converter has two functional modes, namely, shoot-through and non-shoot-through. The circuit diagram of the 21-level QZS-CHBMLI is shown in Figure 2. In the non-shoot-through state, the inverter behaves as a regular H-Bridge inverter, and the derivations for i_{lk} and V_{ck} for each respective cell, with k denoting the cell number, is gotten from equations (1) and (2).

$$C_k \frac{dV_{ck}}{dt} = -i_{lk} \tag{1}$$

$$i_{lk} \frac{dV_{lk}}{dt} = -V_{ck} \tag{2}$$

where, C_k represents the capacitance of the $k-th$ cell, V_{ck} represents voltage across the capacitor of the $k-th$ cell, and i_{lk} represents the inductor current of the $k-th$ cell. The mathematical representations of the equations governing this state are expressed in equations (3) and (4).

$$i_{lk} \frac{dV_{ck}}{dt} = -i_{ck} \tag{3}$$

$$L_k \frac{di_{lk}}{dt} = V_{lk} \tag{4}$$

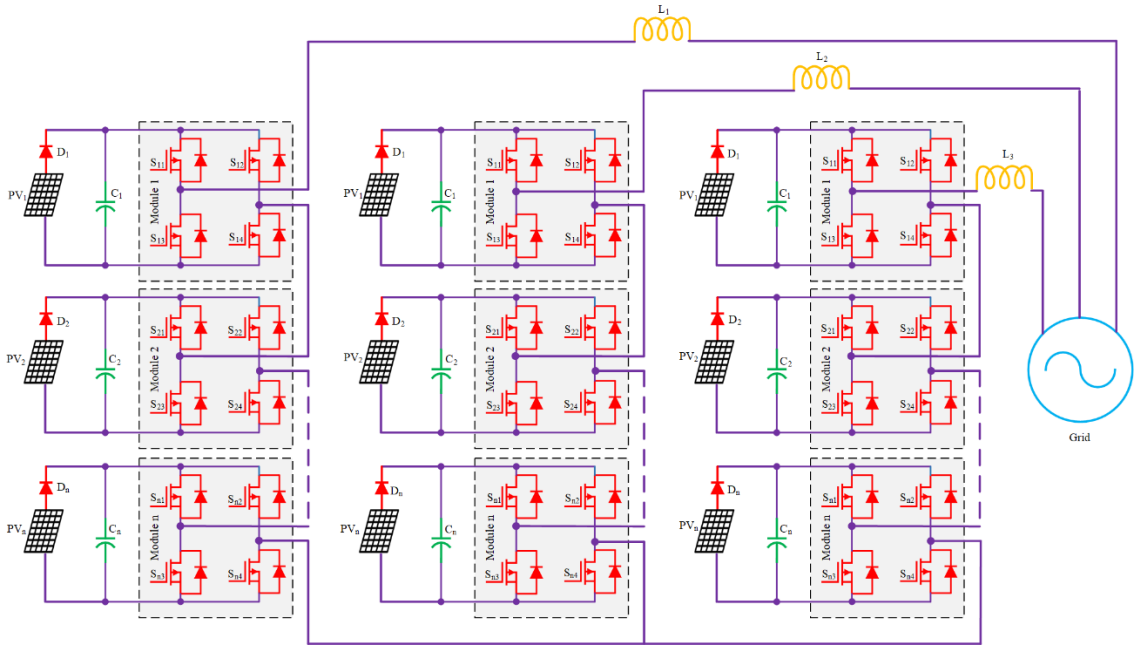

.

Figure 2: circuit diagram of 21 level QZS-CHBMLI

The result voltage V_{out} is represented as follows:

$$V_{out}(t) = L_f \frac{di_f(t)}{dt} + r_f i_f(t) + V_{grid}(t) \tag{5}$$

where, $V_{out}(t)$ represents the output voltage, L_f represents the filter inductance, $i_f(t)$ represents the filter current, r_f represents the resistance of the filter, $V_{grid}(t)$ represents the grid voltage. Consider T_s as one switching cycle, T_{sh} as the period of time when this switches its control to shoot through, and T_{ns} as the interval of a shoot-through. Its connection is $T_{sh} + T_{ns} = T_s$. Where the shoot-through duty cycle is expressed mathematically as $D_{sh} = \frac{T_{sh}}{T_s}$. Steady state, voltages across the capacitor, Peak voltage and DC-link voltage V_{dc} is calculated as per equation (6).

$$\begin{cases} V_{c1} = \dfrac{V_{in}(1-D_{sh})}{D_{sh}} \\ V_{c2} = \dfrac{V_{in}(1-D_{sh})}{1-D_{sh}} \\ \hat{V}_{dc} = V_{c1} + V_{c2} = \dfrac{V_{in}}{1-D_{sh}} - B \end{cases} \quad (6)$$

where, V_{c1} and V_{c2} represents the capacitor voltages, the input voltage is denoted by V_{in}, D_{sh} represents the shoot-through duty ratio, DC-link voltage is denoted by V_{dc}, the peak DC-link voltage is denoted by $\hat{V}_{dc}$, B denotes the additional voltage component. The switching variable S_{km} has to be controlled as follows

$$V_{out} = V_{dc} S_{km} - \sum_{k=1}^{n} i_k \quad (7)$$

where, S_{km} represents the switching variable for cell k and switch m, the total number of cells is denoted by n.

$$N_{total} = 2^m \quad (8)$$

where, N_{total} represents the total number of switching signal combinations. In addition to these, there are three more switching states that show up during shoot-through states. These combinations of switches occur when both switches on the same leg are turned on at the same time, either for one of the cells or both.

2.2 Mathematical Modelling of Fractional Order Notch Filter (FONF)

The notch filter is designed mainly to reject unwanted frequencies from the signal, with very high strength at a specified frequency. Such a notch filter is said to be a selector or rejector in many applications as it behaves as a simple band-pass or band-reject. The integer-order notch filters and some other have the limitation of having a fixed time period in the case of the integrator or differentiator. However, fractional-order control theory is taken into consideration for flexibility and merits apart from being led to the construction of fractional-order filters which offer more options of modifying the fixed shape of integer order filters because of the issues in integer-order filters.

$$G(s) = \frac{s^2 + \omega_0^2}{s^2 + 2\varsigma\omega_0 s + \omega_0^2} \quad (9)$$

where, ω_0 represents the natural frequency, ς represents the damping factor, s represents the complex frequency variable.

$$F(s) = \frac{s^{\alpha+\beta} + \omega_0^2}{s^{\alpha+\beta} + \omega_n(\varsigma s + \omega_n)} \quad (10)$$

where, α and β represents the fractional order parameters, ω_n represents the characteristic frequency.

$$F(j\omega) = \frac{\omega^{\alpha+\beta} + \omega_0^2}{\omega^{\alpha+\beta} + \omega_n(\varsigma\omega + \omega_n)} \quad (11)$$

where, ω represents the frequency variable. Consequently from the above derivation, though the quality factor of the filter increases, yet none of the fractional orders are found to be as compared with low-frequency responses as their integer-order counterparts.

2.3 Mathematical Modelling of Crested Porcupine Optimizer (CPO)

The population-based algorithm uses Crested Porcupines as search agents to solve optimization problems. In CPO, a CP represents the candidate solution; therefore, there is a periodic update of this candidate solution in the course of optimization. Equation (12) gives the position matrix of the search agents:

$$Z=\begin{bmatrix} Z_1 \\ \vdots \\ Z_i \\ \vdots \\ ZN_{\max} \end{bmatrix}=\begin{bmatrix} z_{1,1} & \cdots & z_{1,j} & \cdots & z_{1,d} \\ \vdots & \ddots & \vdots & \iddots & \vdots \\ z_{i,1} & \cdots & z_{i,j} & \cdots & z_{i,d} \\ \vdots & \ddots & \vdots & \iddots & \vdots \\ zN_{\max},1 & \cdots & zN_{\max},j & \cdots & zN_{\max},d \end{bmatrix} \quad (12)$$

where, Z denotes the population, Z_i represents the $i-th$ individual of population, which is equal to position of $i-th$ candidate solution, and $z_{i,j}$ denotes the position of the $j-th$ dimension of the $i-th$ agent, the maximum number of agents in the population is denoted by $N_{\max}$, the total number of dimensions is denoted by d. At the time of initialization, Y_i would be created randomly within search space using equation (13).

$$Y_i = L + rand \times (U - L), \qquad i = 1, 2, \ldots, N_{\max} \quad (13)$$

where, L and U denotes the lower and upper bounds of the optimization problem, while rand is a randomly generated vector within values ranging between 0 and 1. During the optimization process, the objective function is used to calculate the fitness value of each candidate solution. all individuals are gathered to collect their fitness values in the population of the fitness matrix F_{matrix}. This is defined by Equation 14.

$$F_{matrix}=\begin{bmatrix} F_1 \\ \vdots \\ F_i \\ \vdots \\ F_{N_{\max}} \end{bmatrix}=\begin{bmatrix} f(Y_1) \\ \vdots \\ f(Y_i) \\ \vdots \\ f(Y_{N_{\max}}) \end{bmatrix} \quad (14)$$

where, F represents the matrix which holds all the fitness and f represents the objective function.

3. Result And Discussion

This section analyzes and discusses results about power quality improvement in the grid-integrated solar PV system using the proposed FONF. The performance of the FONF, optimized with the CPO, is simulated in MATLAB and compared with existing methods. The analysis is done using two distinct patterns. The patterns are:

Pattern 1: Analysis of the system performance under partial shading for various irradiance levels [1000 W/m2 700 W/m2 500 W/m2 300 W/m2]

Pattern 2: Closed-system performance under partial shading and fluctuating solar irradiance [450 W/m2 1000 W/m2 350 W/m2 300 W/m2]

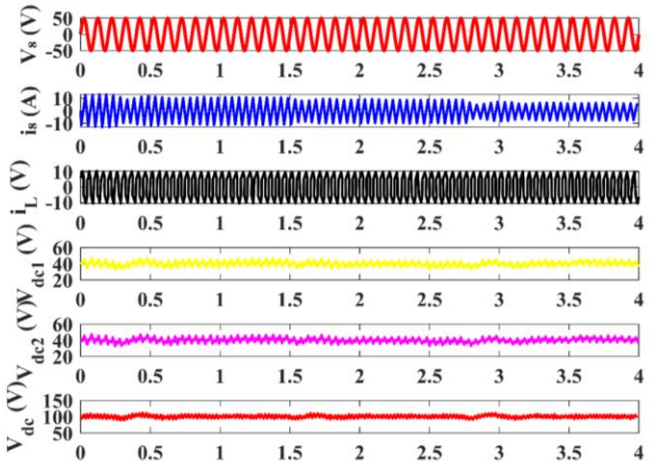

Figure 3: State change of an electrical parameter during the time interval ranging from 0s to 4s for pattern 1

Figure 3 depicts six plots that show the state change of an electrical parameter during the time interval ranging from 0 seconds up to 4 seconds. The first subplot indicates V_s (source voltage) within -50 V, and the second one shows i_s (source current) as it ranges between -10 A and 10 A. The third subplot: i_L (inductor current) ranges between -10 V to 10 V. The fourth and fifth subplots correspond to V_{dc1} and V_{dc2} (DC voltages) changing slightly below 40 V and 60 V, respectively. The last one shows V_{dc} (total DC voltage) -the general total DC across the board-in the range of 100 V with little oscillations.

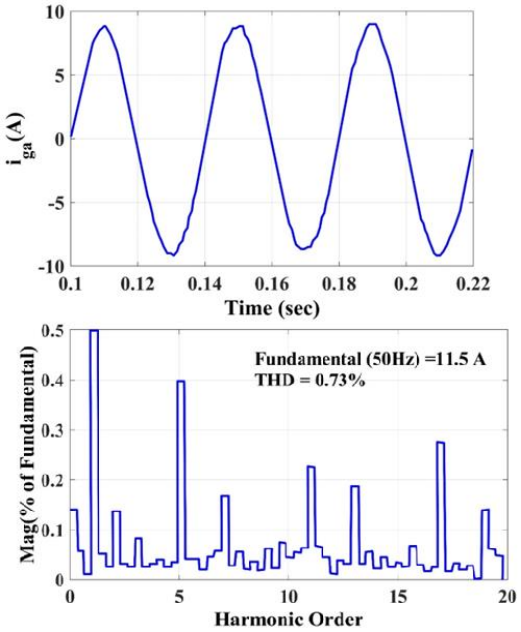

Figure 4: Grid current harmonic spectrum analysis with FONF controller for pattern 1.

Figure 4 shows the current i_{ga} changing between 10 A and -10 A in between the period of 0.1 to 0.22 seconds. It has a pretty well-defined periodic form with peaks at roughly 0.12 seconds and 0.18 seconds. Since the current reaches about maximum 10 A and minimum approximately -10 A, it shows a clearly symmetrical sinusoidal character. The data seem to echo a speedy and steady fluctuation of current in short time. Figure 4 also shows the percentages of the magnitude of harmonics with respect to the fundamental frequency (50 Hz). The major component is recorded at 11.5 A and a Total Harmonic Distortion (THD) of 0.73%. The plot reveals significant peaks at the 5th and 11th order harmonics approximately 0.4 and 0.2, respectively, while most other harmonics are below 0.1. For the overall trend, even though harmonics are present, they are lower compared to the fundamental frequency, illustrating a waveform of good quality with minor distortion.

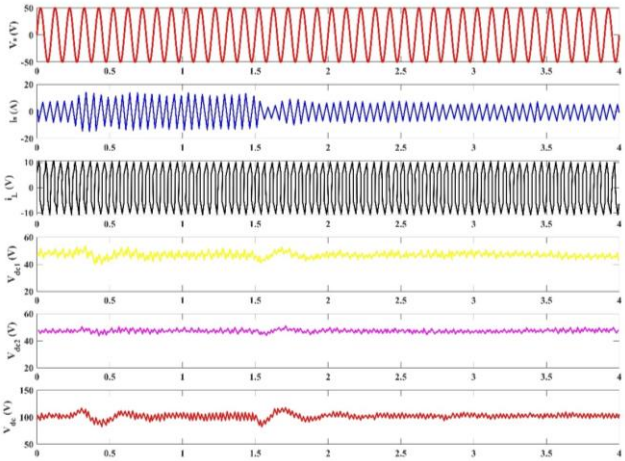

Fig -5: State change of an electrical parameter during the time interval ranging from 0s to 4s for pattern 2

Figure 5 represents six subplots, where six electrical quantities have been depicted with respect to time in the interval of 0 to 4 seconds. In the first subplot, V_s represents source voltage. The amplitude oscillates between -50 V and 50 V. In the second subplot, i_s is plotted that fluctuates from approximately -15 A to 15 A. The third subplot plots i_L which is oscillating from -10 A to 10 A. The fourth subplot shows V_{dc1} as a variation around 40 V, while the fifth subplot indicates V_{dc2} as a fluctuation around 60 V. The sixth subplot indicates V_{dc} as stabilizing around 100 V with minor oscillations.

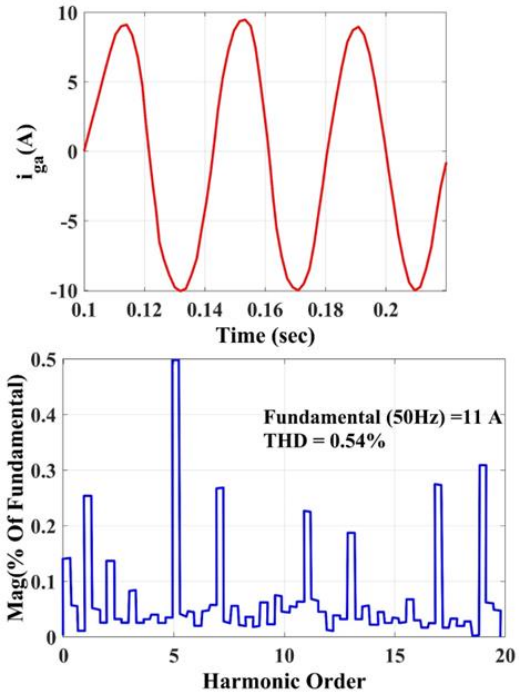

Fig -6: Grid current harmonic spectrum analysis with FONF controller for pattern 2

Figure 6 indicates the current i_{ga} (in A) over time (in sec) between 0.1 to 0.2 seconds. Currents fluctuate between almost 5 A and -5 A, suggesting that there is very nearly a harmonic component, with peaks at around 0.12 sec and 0.18 sec. The fact that it appears sinusoidal indicates a regular frequency and amplitude for the entire time under observation. Thus, broadly speaking, the current fluctuates continuously at a high rate, indicating the dynamic condition of the system in a matter of seconds. Figure 6 also shows the size of harmonics as a percentage of the main frequency (50 Hz) for harmonic orders 1-20. At 11 A, the fundamental component has a THD of 0.54%. The fifth harmonic is characterized by a very large value in these findings, while the other harmonic orders are small in magnitude, generally less than 0.1. This means that the harmonics are minimal with respect to the fundamental frequency, indicating a very good waveform with distinctly low distortion.

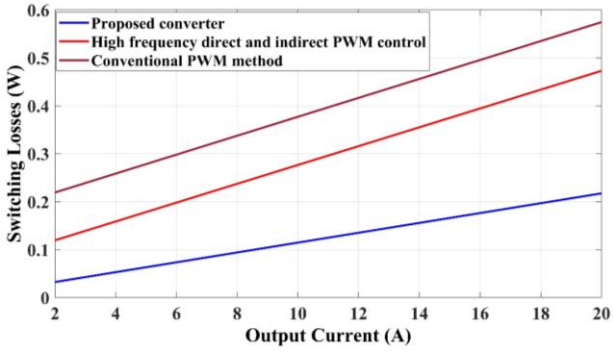

Figure 7: Switching loss vs Output current

Figure 7 shows the switching losses (in W) against output current (in A) for three control methods. The proposed converter increases gradually from around 0.04 W at 2 A to around 0.21 W at 20 A. The high-frequency direct and indirect Pulse Width Modulation (PWM) control starts at about 0.12 W and rises to about 0.48 W at the same output current. The conventional PWM method starts at about 0.2 W and reaches about 0.58 W at 20 A. In general, the proposed converter has the lowest switching losses among the other methods over the output current range.

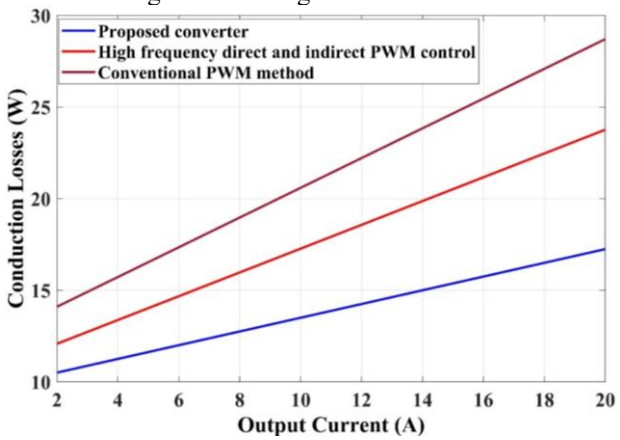

Figure 8: Conduction loss vs Output current

Three distinct control techniques are compared in the relationship between output current (in A) and conduction losses in Figure 8. The proposed converter shows a steady increase in losses, from about 10 W at 2 A to approximately 20 W at 18 A. High-frequency direct and indirect PWM control starts at around 13 W at 2 A and rises to approximately 24 W at 20 A. The conventional PWM method begins at around 15 W and reaches about 29 W at the same current level. Overall, the proposed converter shows lower conduction losses when compared with both other techniques at the output current ranges selected for measurement.

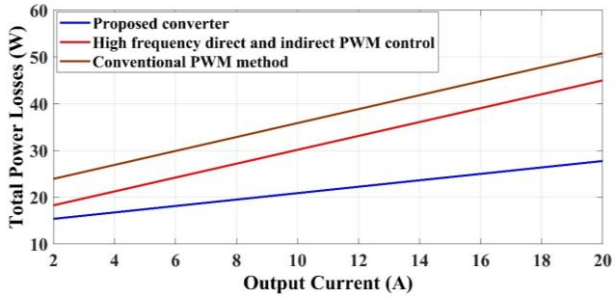

Figure 9: Total power loss vs Output current

In Figure 9, total power loss is shown (in watts) as a function of output current (in amperes) for three methods the proposed converter, high-frequency direct PWM control and indirect PWM control, and conventional PWM. The proposed converter exhibits the lowest power losses starting below 15 watts at 2 A and rising to approximately 29 watts at 20 A. High-frequency PWM control has average losses ranging from 19 watts at 2 A to 45 watts at 20 A. The conventional method of PWM has maximum losses that range from 25 watts at 2 A to 50 watts at 20 A. Showing a clear comparison that proposed converter is the most efficient method with regard to minimizing power losses at the output.

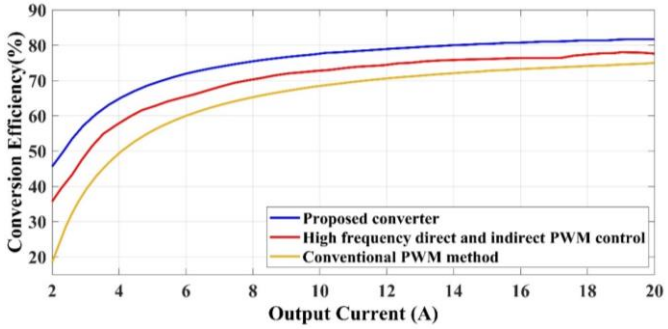

Figure 10: Conversion efficiency

Figure 10 compares conversion efficiencies (%) of three conversion methods-the proposed converter, high-frequency direct and indirect PWM control, and conventional PWM method-with respect to output currents (A). At an output current of 2 A the proposed converter starts about 48%, by high-frequency PWM at around 37% and conventional PWM approximately 20%. With higher output currents up to 10 A, the proposed converter reaches around 78%, high-frequency PWM close to around 72%, and about 68% for conventional PWM. At 20 A, the proposed converter exceeds 82%; high-frequency PWM is approximately 78%; and conventional PWM is approaching 75%. Moreover, across all output currents, the proposed converter consistently demonstrates greater efficiency.

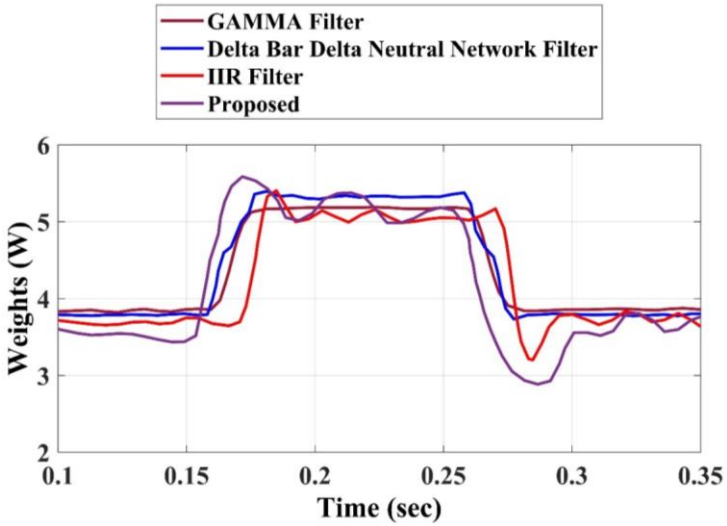

Figure 11: Analysis of filter convergence under dynamic load conditions

In Figure 11, there are comparisons of four filters which are GAMMA Filter, IIR filter, delta bar delta neutral network filter, and a proposed filter. The x-axis shows time measured in seconds, from 0.1 as a minimum to 0.35 as a maximum. The y-axis, on the other hand, is measured in weights or watts, ranging from 2 to 6 watts. The GAMMA Filter and IIR Filter are very similar to each other while reaching a peak of about 5.3 watts at 0.2 seconds. The delta bar delta neutral network filter displays a different and more constant pattern at 4.5 to 5 watts. Peak of above 5.5 watts is attained by the proposed filter where it peaked a little earlier than other filters. In all the filters, similar patterns are observed, namely initial increase, a peak, and then a decline.

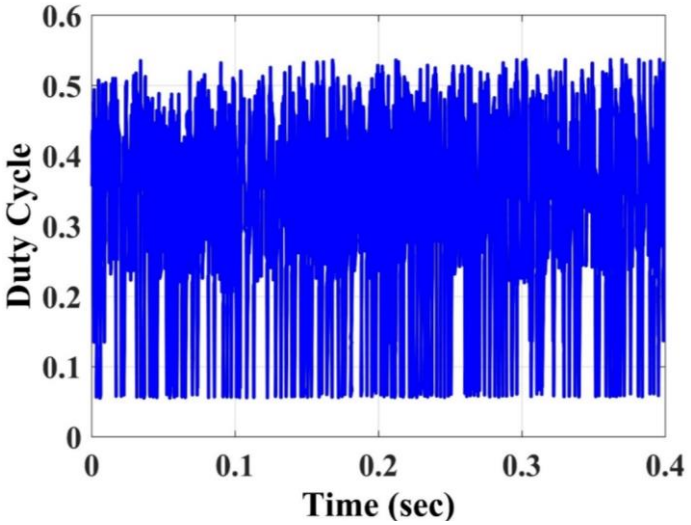

Figure 12: Varying duty cycle of CPO

Figure 12 shows the time period from 0 to 0.4 seconds for duty cycle with some values between roughly 0.1 and 0.5. The patterns of the duty cycle are heavily variable, meaning many changes in its on-off signal state. A large portion of the data lies between 0.2 to 0.3, possibly indicating that it is a mostly low duty cycle. This heavy variability might be pointing towards a rapid switching behaviour or possible noise within the signal.

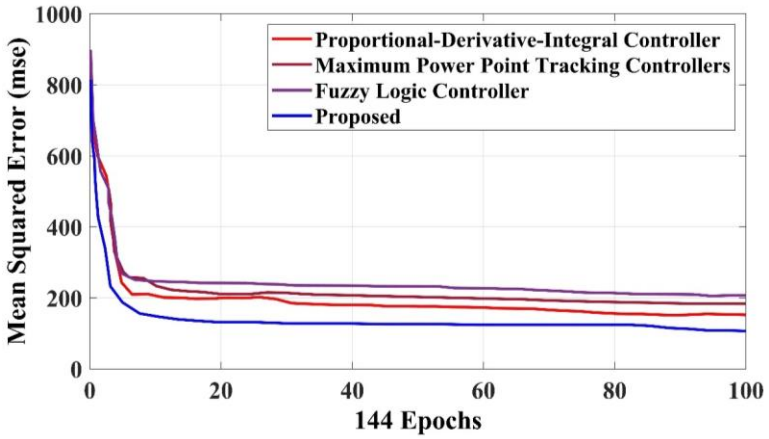

Figure 13: Mean squared error vs Epochs

Figure 13 presents the behaviour of the Mean Squared Error (MSE) of four controllers across 144 epochs. The Proportional-Derivative-Integral (PDI) controller begins with an MSE of almost 800, reduces rapidly to about 150 till the 20th epoch, and gets stabilized at around 200. Both the MPPT controllers and the Fuzzy Logic Controller (FLC) perform in the same way, starting from around 800 and having an almost similar downward movement, ending with values of around 220 and 240 respectively. The proposed controller has a pattern where it begins at about 800 and then rapidly declines to an MSE of nearly 140 by the 20th epoch and then stabilizes at around 50, performing better than the other three controllers.

Table 1: Comparison of various control strategies

Operation	QPR [18]	LQR [18]	ANN [18]	IPT [18]	FO-PFSOGI [18]	Proposed
Type	Adaptive	Adaptive	Neuron-based adaptive technique	Transformer	Fractional order	FONF
Implementation complexity	Moderate	Moderate	Complicated	Less	Moderate	Less
Dynamic response	Fast	Slow	Slow	Slow	Fast	Fast
Harmonic mitigation	5.2%	3%	3.67%	3.12%	2.13%	0.54% (grid current)
DC-link voltage ripples	Not reported	Less	High	High	Less	Less

Table 1 compares different control strategies such as Quasi-Proportional-Resonant (QPR), Artificial Neural Network (ANN), Linear–Quadratic Regulator (LQR), Instantaneous Power Theory (IPT), Fractional order Control theory-based Pole fixed Second Order Generalized Integrator (FO-PFSOGI), and the proposed method based on several criteria. Among all, the proposed method is the best one, having a FONF type with low implementation complexity and fast dynamic response. Harmonic mitigation for the proposed method is much lower at 0.54% (grid current) than that observed in QPR, at 5.2%; LQR at 3%; ANN at 3.67%; IPT at 3.12%; and FO-PFSOGI at 2.13%. At the same time, the proposed method has very low DC-link voltage ripples like LQR and FO-PFSOGI, but way better than the high ripples compared to ANN and IPT. The proposed method has the highest dynamic response and harmonic mitigation and, therefore, is the most efficient one.

Table 2: Performance comparison in terms of computational time, sampling time, and accuracy

Method	Computational time	Sampling time	Accuracy
LLMS [19]	1.78 s	30 µs	97.67 %
PSO [19]	1.28 s	50 µs	98.76 %
ANROA [19]	1.202 s	20 µs	98.86 %
ANF [19]	3.26 s	42 µs	95.23 %
P&O [19]	2.40 s	50 µs	96.56 %
Proposed [19]	0.75 s	13 µs	99.17 %

Table 2 compares the various methods based on computational time, sampling time, and accuracy. As shown in the same table, the method proposed outperforms others in terms of computational time (0.75 s), minimal sampling time (13 µs), and maximum accuracy (99.17%). Leaky Least Mean Squares (LLMS) has a computational time of 1.78 s, sampling time of 30 µs, and accuracy of 97.67%. Particle Swarm Optimization (PSO) has a recording time of 1.28 s, 50 µs, and accuracy of 98.76%, whereas Neuro-Fuzzy Inference System with Rain Optimization Algorithm (ANROA) recorded 1.202 s, 20 µs, and 98.86% accuracy. Adaptive Notch Filter (ANF) had the highest computational time of 3.26 s with a sampling time of 42 µs and 95.23% accuracy. Perturb and observe (P&O) took 2.40 s computing time with 50 µs sampling time and achieving 96.56% accuracy, which makes the proposed method the best one compared to other methods.

4. CONCLUSIONS

This research demonstrated the efficiency of a FONF coupled with CPO for power quality improvement in grid-tied solar PV systems using QZS-CHBMLI. The proposed control strategy could be said to address the major concerns of power quality for harmonic distortion, voltage fluctuation stability, and suspension dynamics concerning renewable energy power plants connected to the grid. The FONF, which acts to eliminate spurious harmonics, considerably reduced THD, while stability of the system is achieved. Use of CPO further fine-tuned the filter parameters, ensuring adaptive viability and high efficiency under varying operating conditions. Together with the QZS-CHBMLI, the system offered a well-built solution for DC-to-AC conversion with high-quality multilevel output and enhanced voltage regulation. MPPT kept optimum energy recuperation from the solar PV array regardless of the changing conditions of loads and solar irradiance. Simulation and experimental results have proved the aptitude of this system in achieving significant improvements in various power quality indices, such as reduced THD and enhanced voltage stability. The synergism of fractional-order control techniques with optimization algorithms is productive in enhancing the technical aspects of renewable energy integration. Hence, the solution FONF-CPO has great prospects for being an effective and extensible solution for power quality improvement in a grid-integration PV system. It indicates the development of more effective, reliable, and sustainable energy systems. Future work address real-time implementation and more scalability.

5. REFERENCES

[1] Kanagaraj, N., Vijayakumar, M., Ramasamy, M. and Aldosari, O., 2023. Energy management and power quality improvement of hybrid renewable energy generation system using coordinated control scheme. *IEEE Access*.
[2] Ibrahim, N.F., Mahmoud, M.M., Al Thaiban, A.M., Barnawi, A.B., Elbarbary, Z.S., Omar, A.I. and Abdelfattah, H., 2023. Operation of grid-connected PV system with ANN-based MPPT and an optimized LCL filter using GRG algorithm for enhanced power quality. *IEEE Access*.
[3] Maurya, J., Saket, R.K. and Srivastava, R.K., 2024. Performance Analysis of Single-Stage and Two-Stage VSI-Fed Induction Motor Drives for Solar Water Pumping Applications. *IEEE Transactions on Industry Applications*.
[4] Prasad, D.A., Muralikrishnan, G., Navaneethan, C. and Meenatchi, S., 2024. A novel modified switched capacitor multilevel inverter using SARC-DQRLC controlling mechanisms for grid systems. *International Journal of Hydrogen Energy*, *77*, pp.40-53.
[5] Kumar, P.M., Priya, N., Dhilipkumar, R. and Krishnan, T.S., 2024. Maximizing solar energy efficiency with efficient interleaved boost converter with three-level neutral point clamped inverter for grid-connected photovoltaic using hybrid approach. *Solar Energy*, *280*, p.112855.
[6] Pawar, V.S. and Gaidhane, P., 2024. A resilient approach for optimizing power quality in grid integrated solar photovoltaic with asymmetric 15-level inverter. *Computers and Electrical Engineering*, *116*, p.109211.
[7] Kumar, R.T. and Rajan, C.C.A., 2023. Integration of hybrid PV-wind system for electric vehicle charging: Towards a sustainable future. *e-Prime-Advances in Electrical Engineering, Electronics and Energy*, *6*, p.100347.
[8] Sunil Kumar, C., Puttamadappa, C. and Chandrashekar, Y.L., 2023. Power quality improvement in grid integrated PV systems with SOA optimized active and reactive power control. *Journal of Electrical Engineering & Technology*, *18*(2), pp.735-750.
[9] Ismeil, M.A., Abdel-Rahim, O., Hussein, H.S. and Abdelhameed, E.H., 2023. Implementation of New Optimal Control Methodology of Quazi Z-Source Inverter Based on MPC. *IEEE Access*, *11*, pp.56453-56462.
[10] Gupta, S., Gill, A. and Singh, M., 2023, January. Power quality enhancement using active shunt harmonic filter based on PV. In *2023 International Conference on Intelligent and Innovative Technologies in Computing, Electrical and Electronics (IITCEE)* (pp. 302-307). IEEE.
[11] Srinath, N.S., Sundarabalan, C.K., Sharma, J., Balasundar, C. and Vijayakumar, V., 2023. Quasi newton least mean fourth control for multifunctional grid tied solar photovoltaic system. *Sustainable Energy Technologies and Assessments*, *57*, p.103272.

[12] Anusha, G., Arora, K., Sharma, H., Thota, S.P., Joshi, G.P. and Cho, W., 2024. Control strategies of 15-level modified cascaded H-bridge MLI with solar PV and energy storage system. *Energy Reports*, *12*, pp.2-26.
[13] Bhimraj, M.R. and Susitra, D., 2024. Mitigate power quality issues in PV solar inverter using hybrid optimized light GBM-based controller. *Electrical Engineering*, pp.1-15.
[14] Kumar, P.S.S., Suresh, P. and Lenine, D., 2024. Performance improvement of predictive voltage control for interlinking converters of integrated microgrid. *Measurement: Sensors*, *33*, p.101196.
[15] Rajamallaiah, A., Karri, S.P.K., Alghaythi, M.L. and Alshammari, M.S., 2024. Direct Current Control of Grid Connected Two Level Inverter With LCL-Filter Using Deep Reinforcement Learning Algorithm. *IEEE Access*.
[16] Badoni, M., Singh, A., Pandey, S. and Singh, B., 2021. Fractional-order notch filter for grid-connected solar PV system with power quality improvement. *IEEE Transactions on Industrial Electronics*, *69*(1), pp.429-439.
[17] Bansal, P. and Singh, A., 2024. Solar PV integrated simplified multilevel inverter configuration for power quality improvement using multilayer Gamma filter. *Electrical Engineering*, pp.1-17.
[18] Badoni, M., Singh, A., Tripathi, R.N., Kumar, R. and Singh, V.K., 2024. Fractional order pole fixed second order generalized integrator based control for grid connected solar photovoltaic system. *IET Power Electronics*.
[19] Prasad, D., Kumar, N., Sharma, R., Malik, H., Márquez, F.P.G. and Pinar-Pérez, J.M., 2023. A novel ANROA based control approach for grid-tied multi-functional solar energy conversion system. *Energy Reports*, *9*, pp.2044-2057.